Microsystem Technologies
https://doi.org/10.1007/s00542-021-05217-0

TECHNICAL PAPER

Maskless lithography: an approach to SU-8 based sensitive and high-g Z-axis polymer MEMS accelerometer

Mandeep Jangra[1,2] · **Dhairya Singh Arya**[1,3] · **Robin Khosla**[1,4,5] · **Satinder K. Sharma**[1,6]

Received: 13 September 2020 / Accepted: 3 April 2021

Abstract

In this work, Z-axis MEMS accelerometers are investigated with variation in spring topography. The serpentine spring structure demonstrated the optimum sensitivity of MEMS accelerometers due to a large number of beams that reduce the spring constant considerably. The augmented serpentine spring MEMS accelerometers are simulated for SU-8, PolySi, Si_3N_4, and SiC-based primary structural materials. SU-8 based MEMS accelerometer shows high sensitivity and cost-effective fabrication process suitable for industry. The reliability of the microaccelerometers is investigated by the stress analysis. The computation result of designed accelerometers exhibited a linear response up to $\pm$ 50 g of the input value of acceleration. For the integration with Si-technology, SU-8 microaccelerometer with serpentine spring structure is fabricated using facile maskless lithography based grayscale process technology. The sensitivity is measured by capacitance variation with Z-axis free falls. The frequency response and spring constant of fabricated SU-8 based Z-axis MEMS accelerometer is investigated by Laser Doppler Vibrometer and nanoindentation technique, respectively. The demonstrated SU-8 serpentine spring, highly sensitive, facile and low-cost process technology-based Z-axis accelerometer is suitable for navigation, space, and medical applications.

1 Introduction

Microelectromechanical systems (MEMS) accelerometers are widely adopted in automotive, robotics, consumer, biomedical, military, and space applications (Yazdi et al. 1998; Alvin Barlian et al. 2009). MEMS accelerometers are primarily classified into capacitive, piezoelectric, and piezoresistive accelerometers based on their transduction mechanism (Narasimhan et al. 2015; Roy and Bhattacharyya 2015; Kobayashi et al. 2011; Zhou et al. 2015). From these, the capacitive MEMS accelerometers have attracted immense attention owing to high resolution, temperature, long-term stability, and simple batch fabrication process technology (Zhou et al. 2015). MEMS accelerometers measure the capacitance change between a stationary electrode fixed to the substrate and a movable electrode on a suspended proof mass (Kumar et al. 2016). Additionally, the capacitive sensing scheme is also suitable for standard close loop operation, where electrostatic feedback is used. Presently, most of the fabrication interfacing techniques are in general more accessible for the high-resolution conversion of analog to digital domain, which is by and large electromechanical Sigma-Delta Modulators ($\Sigma\Delta$M) (Chen et al. 2016).

✉ Satinder K. Sharma
satinder@iitmandi.ac.in

Dhairya Singh Arya
dhairya_arya@yahoo.in

Robin Khosla
robin@ece.nits.ac.in

1 School of Computing and Electrical Engineering (SCEE), Indian Institute of Technology (IIT)-Mandi, Mandi, Himachal Pradesh 175005, India

2 Present Address: Indian Institute of Technology (IIT), Roorkee, India

3 Present Address: Centre for Applied Research in Electronics (CARE), Indian Institute of Technology (IIT), Delhi 110016, India

4 Present Address: Institut für Halbleitertechnik, Universität Stuttgart, Pfaffenwaldring 47, 70569 Stuttgart, Germany

5 Present Address: Department of Electronics and Communication Engineering (ECE), National Institute of Technology (NIT), Silchar, Assam 788010, India

6 Present Address: School of Computing and Electrical Engineering, Indian Institute of Technology (IIT), Mandi, Himachal Pradesh 175005, India

Published online: 29 April 2021

An ideal high-performance MEMS accelerometer requires high sensitivity, large bandwidth, reasonable working range as per the application, and low-cost straightforward fabrication process technology (Michel 2004). Numerous MEMS accelerometer designs are investigated in literature (Fan et al. 2020; Ahmed et al. 2020; Taghavi et al. 2019; Liu et al. 2015; Suzuki and Tai 2006; Hurst et al. 2015; Llobera et al. 2007; Carreno et al. 2013; Xie and Fedder 2000; Zhao et al. 2007; Qu et al. 2008; Paul et al. 2008; Milligan et al. 2011; Mohamad 2010; Roylance and Angell 1979), but with limited sensitivity, complicated process, and high fabrication cost. Therefore, other potential design structures for MEMS accelerometers are worthy of investigation. Besides this, the optimum performance of a MEMS accelerometer is also extensively dependent on the structural material of the accelerometer. In literature, PolySi, Si_3N_4, SU8, and SiC-based structural materials are investigated up to a certain extent, but with low sensitivity and high cost due to use of conventional expensive micromachining process technology (Kwon and Park 1998; Lapadatu et al. 1996; Jeong and Wang 2004; Rajgopal et al. 2009; Jiang and Cheung 2009; Lawes 2007). In fact, polymer-based MEMS are depicted using grayscale lithography, or SU-8 based MEMS are portrayed using complex and expensive micromachining processes. To the best of author's knowledge SU-8 based Z-axis MEMS accelerometers are not demonstrated with active metal electrodes for electrostatic actuation (Madou 1997; Kim and Meng 2016).

Generally, Capacitive MEMS accelerometers are single or dual-axis. Therefore, two or three accelerometers are integrated for three-dimensional sensing of acceleration, which results in a large area and high cost. The performance of such accelerometers is limited due to the difficulty in the fabrication of the capacitor for measuring out-of-plane movement (Z-axis) as compared to the capacitor for measuring in-plane movement (XY-axis) (Yang et al. 2004; Monajemi and Ayazi 2006). Moreover, these accelerometers have performance limitations due to thin-film structures and involve a complicated fabrication process. Therefore, the investigation of high-performance Z-axis microaccelerometers is highly anticipated (Qu et al. 2004).

In this paper, the Z-axis MEMS accelerometers are designed and simulated with serpentine spring topology using COMSOL 5.4 as FEM (Finite Element Modelling) tool. Designed MEMS accelerometer is examined with variation in structural materials, i.e., SU-8, PolySi, Si_3N_4, and SiC. Here, 50 g acceleration was used for comparison of different proof mass materials to ensure the reliability of the devices so that the stress generated doesn't exceed the yield point. The stress analysis of the accelerometer is presented at ± 50 g. COMSOL Multiphysics with Electro-mechanics and solid mechanics physics are used for the FEM simulations. Whereas for the validation of optimized highly sensitive Z-axis MEMS accelerometer, SU-8 based Z-axis MEMS accelerometer is fabricated by using a facile and low-cost maskless lithography-based grayscale process technology. The frequency response of fabricated SU-8 based Z-axis MEMS accelerometer with serpentine spring structure is investigated by Laser Doppler Vibrometer (LDV) of Polytech MSA-500. The young's modulus of fabricated SU-8 microaccelerometer is investigated by the nanoindentation technique of Hysitron TI 950, TriboIndenter using a Berkovich diamond indenter tip.

2 Materials and methods

2.1 Simulation

Device structure and design used for Finite Element modelling is shown in Fig. 1a. Proof mass dimensions (L × W × H) were assumed to be 1500 μm × 1500 μm × 20 μm for high sensitivity at reasonable dimensions. A 100 nm thin layer of aluminium over moveable hanging proof mass act as upper capacitive electrode for MEMS accelerometer. A thin layer of aluminium of same dimensions on the substrate is considered for lower electrode so that upper electrode overlaps the lower electrode. Since,

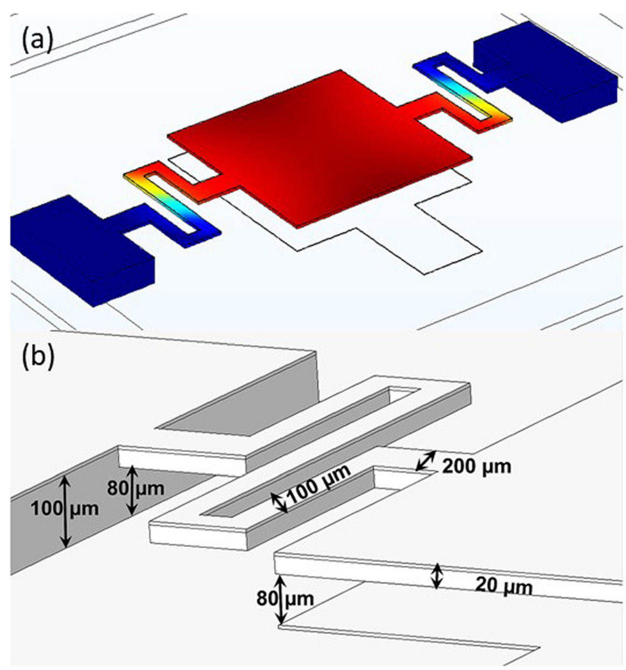

Fig. 1 **a** Micro accelerometer deign with serpentine spring topology, upper electrode has same dimensions as lower electrode so it overlaps completely, **b** detailed dimensions are marked in figure to clarify the dimensions of the design. Serpentine spring are wider near anchor and proof mass connection.

Serpentine spring act as more willing to comply than a fixed straight beams spring of the same length. Serpentine spring topology has very high displacement sensitivity, so it is considered for simulation and comparative study of structural materials. It must be noted that in the serpentine spring structure the proof mass shows buckling. Thus, to minimize buckling in serpentine spring topology, the part of spring connected to anchor and proof mass is kept wider which also enhances mechanical reliability of the structure, and its corresponding dimensions are shown in Fig. 1b.

2.2 Experimental

2.2.1 Fabrication Process

The fabrication of MEMS microstructures using conventional fabrication methods such as bulk and surface micromachining is a complicated and time-consuming process. In this work, one step maskless grayscale lithography is used for the fabrication of SU-8 MEMS accelerometer, which doesn't require the additional cost of physical masks. Instead, Soft masks are made using Microsoft "MS Paint" application, which gives the flexibility of fabricating 3D structures using a grayscale image with ease and at low cost (Rammohan et al. 2011).

Figure 2. shows the process flow used for fabrication of the Z-axis SU-8 microaccelerometer with serpentine spring structure. Initially, p-Si < 100 > substrates were cleaned with standard Radio Corporation of America (RCA) cleaning followed by N_2 dry, dehydration bake at 200 °C for 5 min, and cooled down to room temperature. Subsequently, Al thin film ($\sim$ 100 nm) was deposited using a thermal evaporator at an ultrahigh vacuum of $\sim 3 \times 10^{-6}$ mbar (Fig. 2a). Further, SU8-2002 (MicroChem) photoresist was spincoated using the two-step method: (i) spreading cycle at 500 rpm for 10 s, and (ii) spinning cycle at 3000 rpm for 20 s. After this, the samples were soft-baked from room temperature (RT) to 95 °C for 10 min to evaporate the solvent and then cooled back to RT. After soft bake, the samples were exposed to maskless lithography of Intelligent Micro Patterning SF-100 using Level-1 binary soft mask (Fig. 2b) followed by post-exposure bake (PEB) from RT to 105 °C for 10 min and cooled down to RT, to harden/crosslink the exposed SU-8 region. After this, SU-8 developer (MicroChem) was used for the development of SU-8 patterns for 1 min trailed by IPA rinse and N_2 dry. To pattern the bottom Al contact (Fig. 2c) the samples were etched using standard Al etchant (DI water (1): Acetic Acid (2): Nitric Acid (2): Orthophosphoric acid (10)) at 35 °C for 10–15 min with constant stirring ($\sim$ 100 rpm) followed by DI rinse, N_2 dry. After this, SU-8 is stripped in n-Methyl-2-pyrrolidone (NMP), at 75 °C for $\sim$ 45 min with 14 constant stirring ($\sim$ 100 rpm) followed by DI rinse, IPA, DI rinse and N_2 dry (Soni et al. 2016). Subsequently, the SU-8 2025 photoresist (MicroChem) was spin-coated on the samples at 1000 rpm for 10 s, followed by soft bake from RT to 95 °C for 10 min and cooled down to RT. After soft bake, the samples were again exposed to maskless lithography with level-to-level exposure using Level-2 binary Soft Mask to create anchor points (Fig. 2d) and reliably control the gap between the proof mass and the bottom electrode of final MEMS Structure. This is followed by PEB from RT to 105 °C for 10 min and cooled down to RT, to crosslink the exposed SU-8 anchor points and development for 1 min trailed by IPA rinse and N_2 dry. The samples are then hard-baked at 120 °C for $\sim$ 20 min to harden the anchor points. Further, the SU-8 2025 photoresist was spin-coated again on the samples at 1000 rpm for 10 s, followed by soft bake from RT to 70 °C for 10 min and cooled down to RT. Here, an optimum temperature of 70 °C was used to facilitate the surface micromachining in the development process itself. Higher temperatures result in exertion in the development process, whereas lower temperatures affect the Grayscale exposure to be used in the next step. Subsequently, the samples were exposed to maskless grayscale lithography using serpentine spring structure Grayscale Level-3 Soft Mask (Fig. 2e). Here, grayscale intensity of 0, 130, and 255 was used for unexposed, partially exposed (hanging structure), and fully exposed (anchor points), respectively. This is again followed by PEB from RT to 105 °C for 10 min and cooled down to RT, to harden/crosslink the exposed SU8 region. After this, SU8 developer was used for the development of SU-8 patterns (Fig. 2f) for $\sim$ 2 h trailed by IPA rinse. The samples are then dried in a vacuum desiccator to avoid stiction of proof mass to the bottom electrode. Further, for hard bake of the proof mass, the samples are annealed in a three-zone tube furnace at $\sim$ 150 °C for $\sim$ 20 min to avoid buckling of proof mass due to thermal gradient. Ensuing this, the poly-methyl-methaacrylate (PMMA) photoresist is coated on the samples as a sacrificial layer such that it stays below the proof mass and enables lift-off in further steps (Fig. 2g). Again, Al thin films ($\sim$ 100 nm) were deposited using thermal evaporator at an ultrahigh vacuum of $\sim 3 \times 10^{-6}$ mbar to form the top electrodes (Fig. 2h). Finally, for Lift-off, the samples were dipped in acetone for $\sim$ 20–30 min to complete the Z-axis SU-8 microaccelerometer (Fig. 2(i)) with serpentine spring structure (Fig. 3) followed by DI, IPA, DI Rinses, and dried in a vacuum desiccator. Further to avoid stiction during lift-off process one may use aligned shadow mask for the formation of top aluminium electrode.

Figure 3 shows the side view of the fabricated SU-8 microaccelerometer with serpentine spring structure showing the bottom electrode, spring, and proof mass.

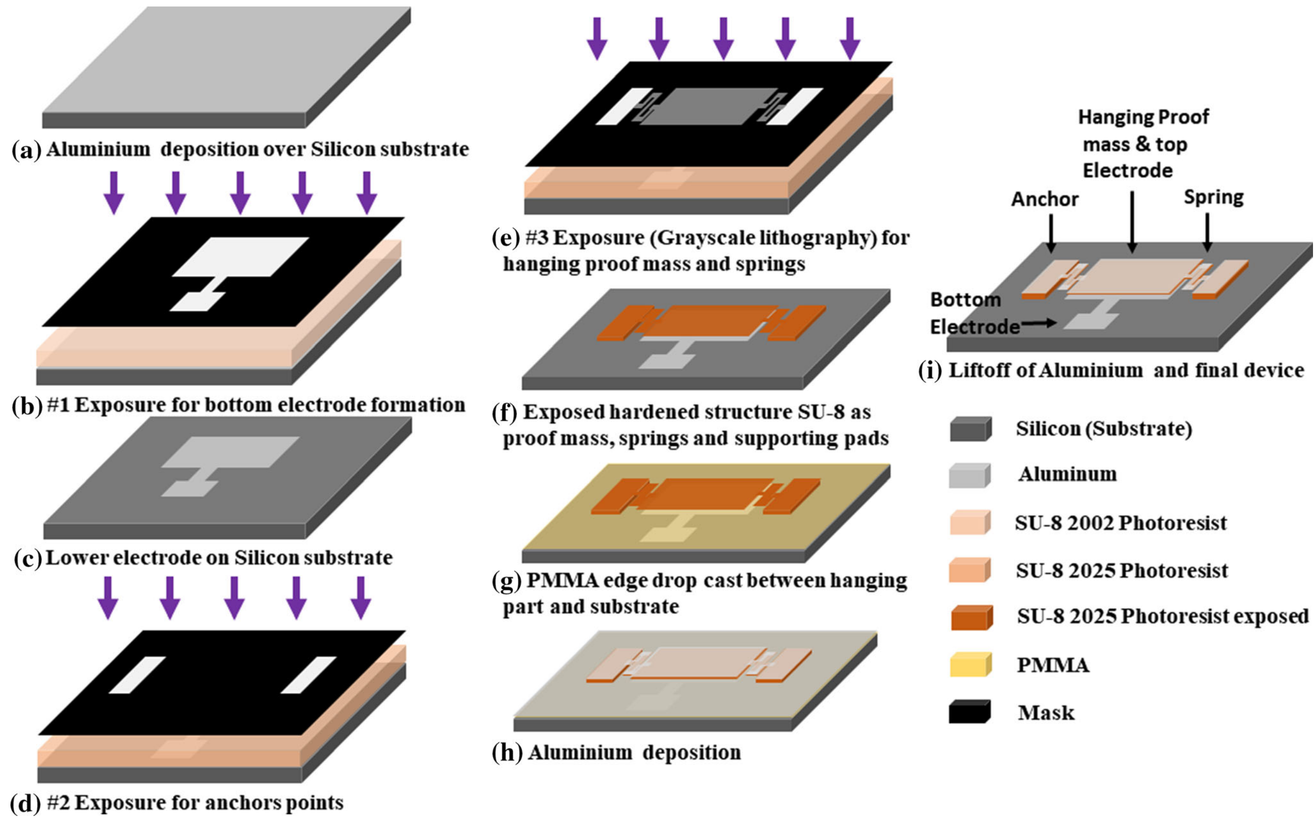

Fig. 2 Process Flow for the fabrication of microaccelerometer, **a** deposition of aluminium for lower electrode, **b** lithography process for lower electrode formation, **c** lower electrode structure on a silicon substrate, **d** binary exposure for the formation of anchor points **e** grayscale lithography process including mask design for hanging structure (black intensity is 0 to block UV light, white intensity is 255 for the anchor and grayscale intensity level is 130 for the hanging part), **f** hanging structure formed with grayscale lithography process, **g** a sacrificial layer of PMMA is edge drop casted to protect the lower electrode in the subsequent liftoff process, **h** aluminium deposition for the formation of top electrode, (**i**) liftoff of aluminium and final device structure

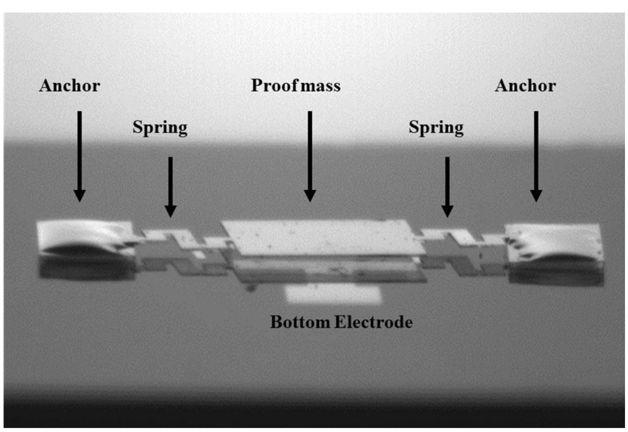

Fig. 3 Side view of the fabricated SU-8 Microaccelerometer with serpentine spring structure. Hanging Proof mass and Spring topology can be seen clearly in this figure

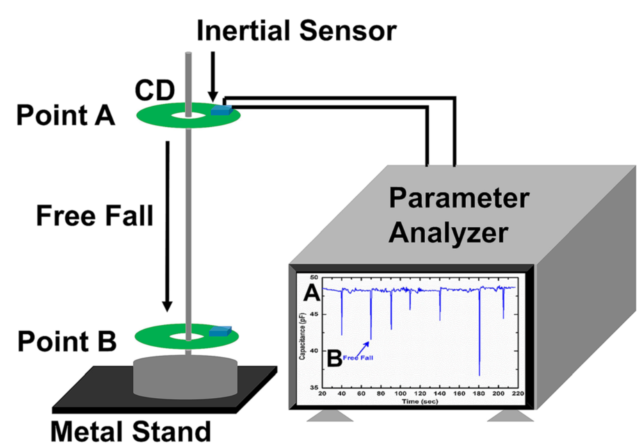

Fig. 4 Setup for measurement of device performance, device fixed on compact disc is freely dropped from point A to point B and variation in capacitance is recorded in parameter analyzer

Here, the top electrode is deposited on the top surface of proof mass which is in contact with the top of springs and supporting anchor pads on the edges.

2.2.2 Characterization setup

Figure 4 shows the setup used for performance analysis of SU-8 microaccelerometer. Here the SU-8 microaccelerometer enclosed in a sample box is fixed on a compact disc. The contact wires are attached to the accelerometer using the silver paste. The contact wires are further connected to the Keithley SCS 4200 electrical parameter analyzer and probe station. For the characterization, the Microaccelerometer is dropped freely from Point A to Point B as shown in Fig. 4, where the distance between Point A and Point B is $\sim$ 40 cm. Resulted change in variation in capacitance is recorded with time for multiple dropping of MEMS accelerometer. Which is further discussed in experimental results of the next section.

3 Results and discussion

3.1 Simulation result

The spring constant is computed from the slope of Force–Deflection characteristics in which a vertical force up to 100 µN is applied on the proof mass (Structural material SU-8 during simulation) and resultant displacement in z-direction is recorded as shown in Fig. 5a (Bao 2000). Computed spring constant for structure give in Fig. 1) is 8.42 N/m. The different materials along with their simulation parameters are shown in Table 1. Here Young's modulus of SU-8 ($\sim$ 4.03 GPa) structural material is estimated using Nano-indentation technique. Using these parameters, the mass of proof mass for SU-8, Poly-Si, Si_3N_4, and SiC materials is calculated to be $\sim 54 \times 10^{-9}$, $\sim 104 \times 10^{-9}$, $\sim 140 \times 10^{-9}$, and $\sim 144 \times 10^{-9}$ kg, respectively.

Figure 5b shows the displacement and acceleration behaviour of SU-8, Poly-Si, Si_3N_4, and SiC structural materials based accelerometers with serpentine spring structural design used for displacement sensitivity computation. Here, the displacement sensitivity is defined by the difference of displacement values at + 50 g and -50 g divided by the total acceleration (100 g). The displacement sensitivity is calculated to be $\sim$ 357.68, $\sim$ 12.50, $\sim$ 11.33, $\sim$ 4.18 nm/g for SU-8, Poly-Si, Si_3N_4 and SiC structural materials based accelerometers respectively. The high displacement sensitivity of SU-8 structural material may be due to low young's modulus as compared to Poly-Si, Si_3N_4, and SiC materials as summarized in Table 1.

For reliability analysis of spring topology, it is necessary to investigate the effect of stress on the spring structures. Von-misses stress is the most popular method for stress analysis of MEMS devices (Hassani et al. 2010; Spearing 2000). In this method, constant acceleration is applied to the device, and corresponding stress generated in the device is measured. Figure 5c shows points of maximum stress on the structure on the geometry of the MEMS accelerometer. The stress generated must be less than the yield point of material for the survival and reliability of the MEMS device. Figure 5d shows the stress vs. acceleration characteristics of SU-8, poly-Si, Si_3N_4, and SiC structural materials based accelerometers with serpentine spring structure. The maximum stress generated at 50 g acceleration for SU-8, poly-Si, Si_3N_4, and SiC structural materials based accelerometers is estimated to be $\sim 2.7 \times 10^6$ N/m^2, $\sim 5.4 \times 10^6$ N/m^2. $\sim 6.9 \times 10^6$ N/m^2, and $\sim 7.2 \times 10^6$ N/m^2, respectively. The stress generated in structural materials is much less than the yield point of $\sim 0.06 \times 10^9$ N/m^2 in the case of SU-8 (Available Online 2021) and $\sim$ 7–14 $\times 10^9$ N/m^2 in case of PolySi, SiC, and Si_3N_4 (Madou 1997). Therefore, the investigated structural materials are reliable for MEMS accelerometer applications.

Furthermore, Fig. 6 shows the frequency response of SU-8, Poly-Si, Si_3N_4, and SiC structural materials based accelerometers with a serpentine spring structure. The resonant frequency of SU-8, Poly-Si, Si_3N_4, and SiC structural materials-based accelerometers is estimated to be $\sim$ 1.39, $\sim$ 4.21, $\sim$ 4.80, and $\sim$ 9.10 kHz, respectively (summarized in Table 2). The reasonable resonant frequency of SU-8 structural material-based accelerometer is due to the high displacement of SU-8, which leads to lower resonant frequency (f_r) as per Eq. (1) and reveals its potential for navigation, space, and medical applications, etc. (Maier-Schneider et al. 1996; Omeltchenko et al. 1996; Kraft 2000).

$$f_r = \frac{1}{2\pi}\sqrt{\frac{F}{mx}} \tag{1}$$

Table 2 summarizes the essential performance parameters of SU-8, poly-Si, Si_3N_4, and SiC structural materials based accelerometers. Table 2 reveals that SU-8 based microaccelerometer is excellently reliable and has the highest displacement sensitivity, reasonable resonant frequency as compared to PolySi, Si_3N_4, and SiC from the simulation analysis. Therefore, SU-8 structural material based structure is used for the fabrication of accelerometer discussed in the next section. Moreover, the SU-8 structural material is highly motivating for use in MEMS applications because of the low-cost fabrication process using three dimensional grayscale Maskless lithography (Rammohan et al. 2011). Therefore, SU-8 structural material is desired for highly sensitive and economical MEMS accelerometer applications.

3.2 Experimental results

The capacitance-time characteristic as measured from the setup (Fig. 4) is shown in Fig. 7. It is observed that there is a sudden decrease in capacitance when SU-8 microaccelerometer is dropped freely from point A to point B.

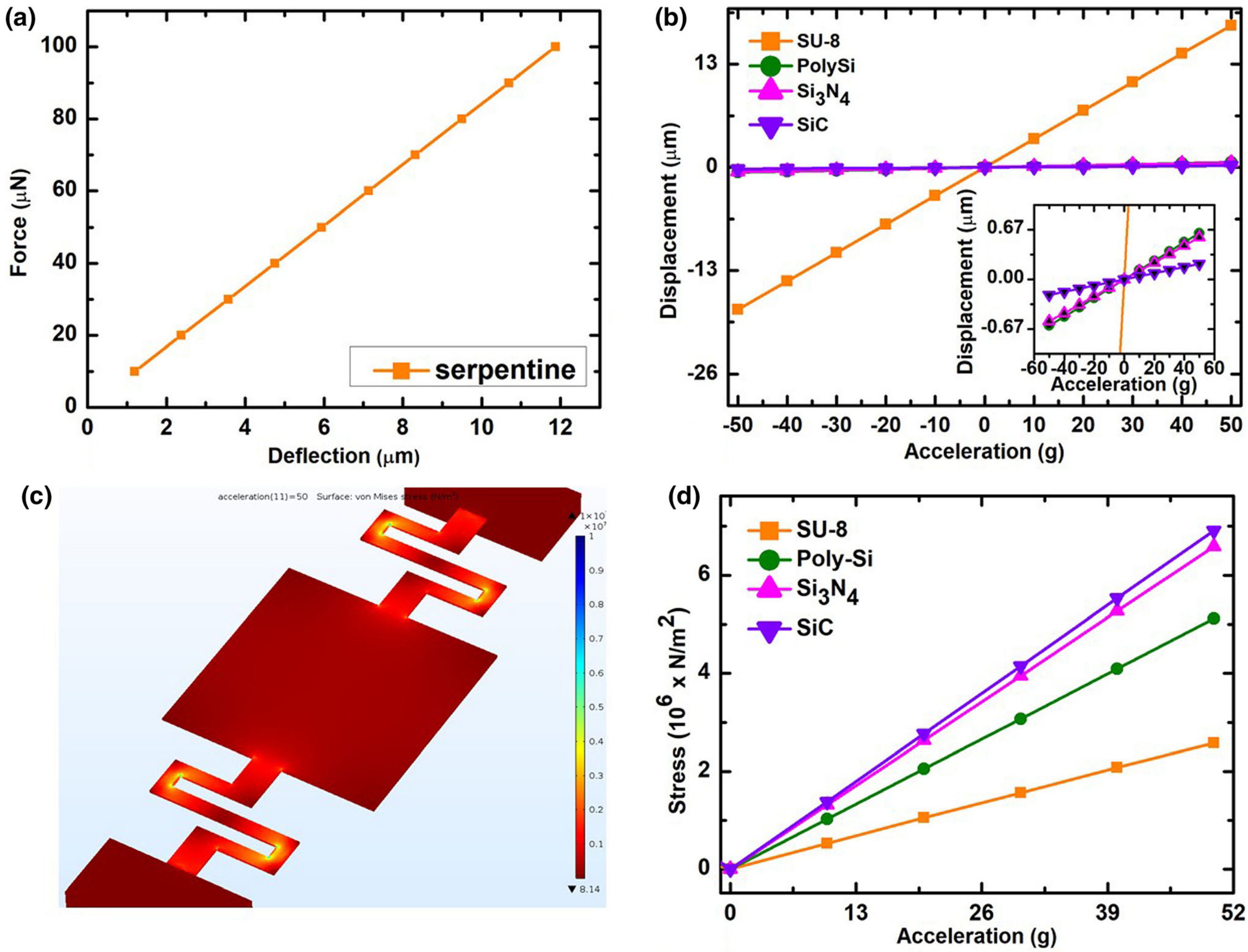

Fig. 5 Simulation results of SU-8, Poly-Si, Si_3N_4, and SiC structural design based accelerometers, **a** force–deflection curve of device structure for the calculation of spring constant (8.42 N/m), **b** Relationship between movable mass displacement and acceleration for SU-8, Poly-Si, Si_3N_4, and SiC structural material based accelerometers, **c** Stress analysis of SU-8, Poly-Si, Si_3N_4 and SiC structural materials based accelerometers, **d** Frequency Response of SU-8, Poly-Si, Si_3N_4, and SiC structural design based accelerometers

Table 1 Comparison of properties of different proof mass materials used for simulation of accelerometer, properties of materials are taken from (Rajgopal et al. 2009; Available Online:Microchem.com; Yi and Kim 1999; Maier-Schneider et al. 1996; Omeltchenko et al. 1996)

Parameter\material	SU-8	Poly-Si	Si_3N_4	SiC
Density (kg/m^3)	1200	2320	3100	3216
Young's modulus (GPa)	4.03	169	250	748
Poisson ratio	0.22	0.22	0.23	0.45

Again, the SU-8 microaccelerometer is taken from point B to point A slowly and held at point A for some time until the capacitance stabilizes. This process is repeated multiple times, and the capacitance drop with various free falls are recorded. Here, the variation in capacitance drop during different free-falls may be due to tilting of microaccelerometer fixed on compact disk while dropping.

In order to validate the frequency response of simulated SU-8 microaccelerometer, it is mandatory to investigate the experimental frequency response. Therefore, the resonance frequency of SU-8 micro-accelerometer with serpentine spring structure is investigated by Laser Doppler Vibrometer (LDV). Figure 8 shows the resonance frequency curve for the fabricated SU-8 microaccelerometer. The experimental results demonstrate the resonance frequency of fabricated micro accelerometer to be $\sim$ 1.35 kHz which is not far off the simulated resonance frequency of $\sim$ 1.39 kHz. In fact, the difference in experimental and simulated resonant frequency (Δf_r) is within the acceptable range of $\sim$ 2.9% (Xie and Fedder 2000), calculated by the following relation:

$$\Delta f_r = \frac{f_{rexp} - f_{rsim}}{f_{rexp}} \quad (2)$$

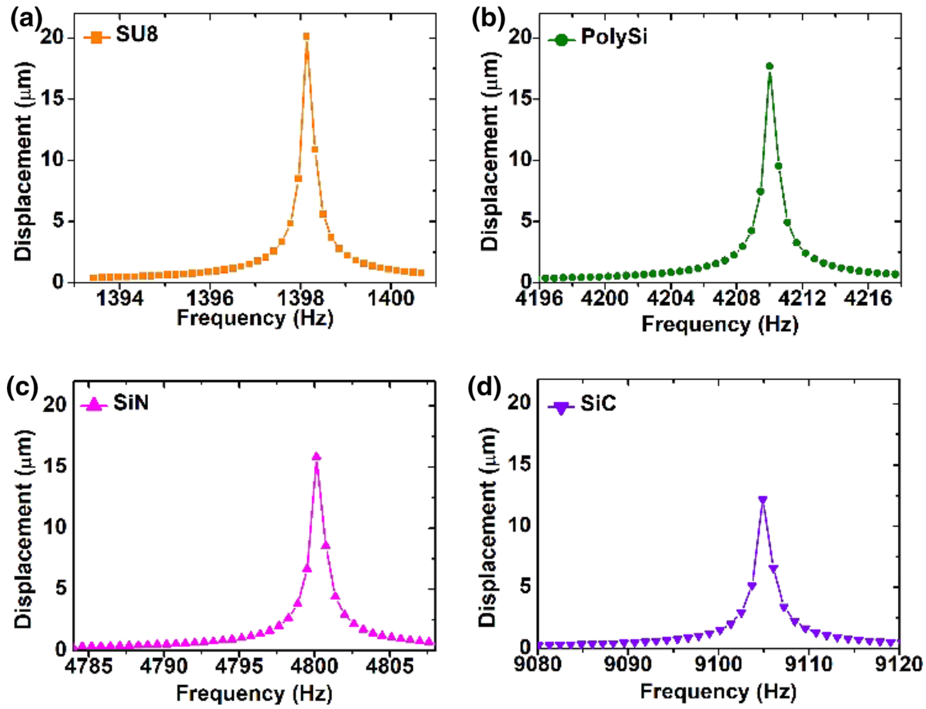

Fig. 6 Frequency Response of **a** SU-8, **b** Poly-Si, **c** Si_3N_4, and **d** SiC structural design based accelerometers

Table 2 Comparison of performance parameters of different proof mass materials in serpentine spring structure

Parameter\material	SU-8	Poly-Si	Si3N4	SiC
Displacement sensitivity (nm/g)	357.68	12.50	11.33	4.18
Resonant frequency (kHz)	1.39	4.21	4.80	9.10
Stress at 50 g ($\times$ 10^6 N/m^2)	2.7	5.4	6.9	7.2

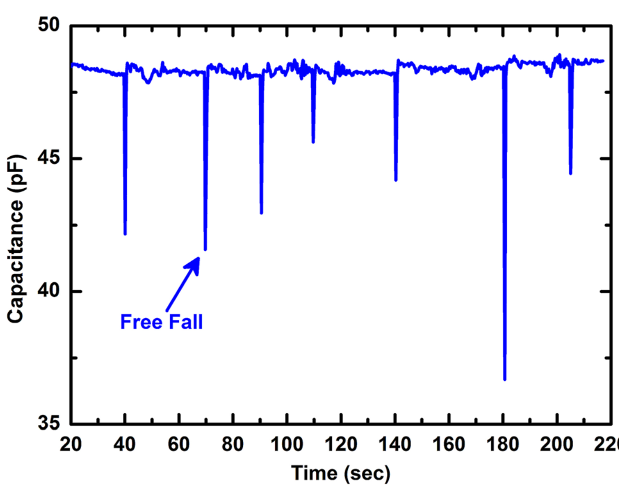

Fig. 7 The trace of capacitance variation generated during free fall of SU-8 microaccelerometer from point A to point B as shown in setup. Spikes shows the fall of MEMS accelerometer at particular time

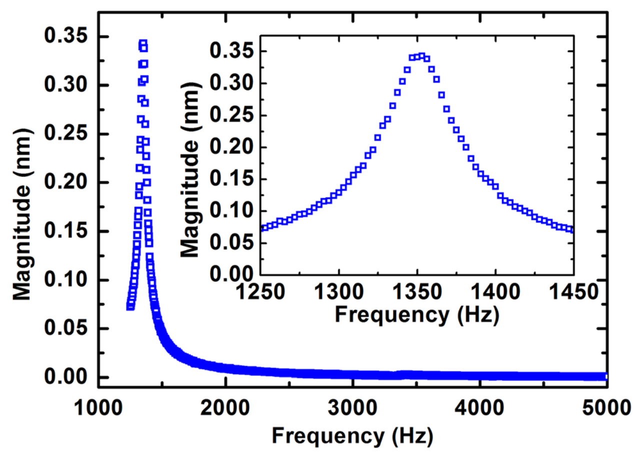

Fig. 8 The resonance frequency curve for the fabricated SU-8 microaccelerometer with serpentine spring structure using LDV. The inset shows the magnified view of the experimental resonance peak

where $f_{\rm rexp}$ and $f_{\rm rsim}$ are the experimental and simulated resonant frequency values, respectively. The trivial variation of $\sim$ 2.9% in experimental and simulation resonant frequency results of microaccelerometer may be due to the process variation of microfabrication technology.

Lastly, from the reliability viewpoint of MEMS devices, the young's modulus is an important parameter for the calculation of resonance frequency. Which is investigated by nanoindentation technique for the exposed SU-8 structural material. Figure 9a shows the load–displacement characteristics of exposed SU-8 material used as a proof mass of microaccelerometer with serpentine spring

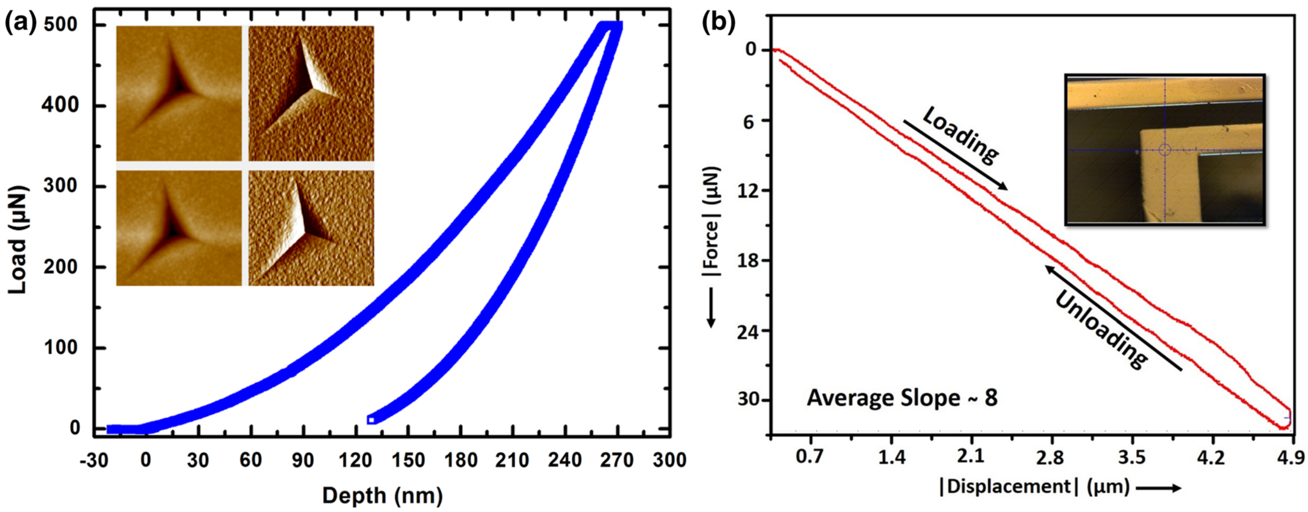

Fig. 9 **a** The Load–Displacement (P–h) for the extraction of young's modulus (4.03 GPa) of SU-8 material exposed with UV. The inset shows the Berkovich diamond indenter tip used for nanoindentation. **b** Force—displacement plot of the fabricated accelerometer for the extraction of spring constant ($\sim$ 8 N/m). The inset indicates the nano-intended point at the suspended serpentine spring.

Table 3 Comparison with state-of-the-art z-axis microaccelerometers

Material	# of masks required	RIE based Process	Releasing	Displacement sensitivity (nm/g)	Resonant frequency (fr) (kHz)	Linear response up to	References
Si/ graphene	2	√	√	–	–	1.5 g	Fan, et al. (2020)
SOI Si	4	√	√	–	2.49	–	Aydemir and Akin (2020)
Si/glass	2	×	√	–	–	–	Rao (2020)
SU-8/carbon black	6	√	√	$\sim$ 280	10.86	–	Seena et al. (2017)
SU-8/carbon black	6	√	×	140	1.88	–	Ahmed et al. (2020)
Steel/PZT	3	×	×	–	4.11	–	Gong et al. (2020)
SU-8	7	×	×	744	0.50	–	Carreno et al. (2013)
SU-8	5	×	√	–	$\sim$ 4	100 g	Jeong and Wang (2004)
SU-8	3 (virtual masks)	×	×	$\sim$ 357.68	$\sim$ 1.35	$\pm$ 50 g	This work

support. Here, the maximum load of 500 µN with contact stiffness of 6.7 µN/nm is applied. The P–h curves reveal the young's modulus of $\sim$ 4.03 GPa for the material used in the fabrication of microaccelerometer which demonstrate high reliability of SU-8 structural material. The physiochemical change in SU-8 from solution ($E_r \sim 2.0$ GPa) to solid structure ($E_r \sim 4.03$ GPa) after UV exposure and Post-Exposure Bake (PEB) altered its mechanical properties (Chung and Park 2013; Oliver and Pharr 2004). Whereas, for experimental computation of the spring constant, the intender tip was bought into contact with the suspended proof-mass of fabricated SU-8 accelerometer and the load was ramped at a constant rate to the desired load and then unloaded. The typical load displacement plot for the fabricated accelerometer is shown in Fig. 9b the spring constant of the fabricated accelerometer is measured from the average slope of the load–displacement plot, and is found to be $\sim$ 8 N/m, which is in great agreement with the simulated result.

Finally, Table 3 summarizes the comparison of the proposed Z-axis SU-8 microaccelerometer with state-of-the-art Z-axis microaccelerometer. This fabricated device in this work shows better sensitivity as compared to other materials. Also the device is economical to fabricate as it does not require complex MEMS processes like surface and bulk micromachining. Also the reported accelerometer covers the wide application areas, such as navigation, space, and medical. Along with high sensitivity, fabrication of this device using grayscale lithography is much simpler and very cost effective.

4 conclusion

The Z-axis MEMS accelerometers is examined for SU-8, PolySi, Si_3N_4, and SiC based primary structural materials. It is acknowledged that SU-8 structural material is desired for highly sensitive and economical MEMS accelerometers. The load–displacement (P–h) curves from nanoindentation revealed the young's modulus of $\sim$ 4.03 GPa for UV exposed SU-8 which ascertains high reliability of SU-8 structural material. Further the force–displacement curve of the fabricated SU-8 accelerometer yields the average spring constant of $\sim$ 8 N/m which is in good agreement with the simulated results. FEM analysis show a linear response up to $\pm$ 50 g of the input value of acceleration. The stress analysis of SU-8 based Z-axis accelerometer shows that stress produced during displacement is much lower than its yield point, thus the structure is quite stable. Thus, the reported polymer MEMS accelerometer with serpentine spring structure and high displacement sensitivity ($\sim$ 357.68 nm/g) is a potential candidate for high-g applications. MEMS accelerometer with SU-8 as a structural material is fabricated using maskless 3D lithography, and capacitance variation with Z-axis free falls is observed. The experimental resonance frequency of fabricated micro accelerometer is estimated to be $\sim$ 1.35 kHz which is within the acceptable range ($\sim$ 2.9%) of simulation value of $\sim$ 1.39 kHz. Therefore, the proposed polymer MEMS accelerometer is cost effective solution for high-g applications.

Acknowledgement The authors acknowledge the Centre for Design and Fabrication of Electronic Devices (C4DFED), sate of the art nanofabrication and characterization facilities at Institute of Technology (IIT), Mandi, Himachal Pradesh, 175005, India for fabrication and characterization of devices. S.K.S. acknowledge the financial support of seed Grant Project IIT/SG/SKS/27, Indian Institute of Technology (IIT), Mandi, Himachal Pradesh, India. The authors also thank Central Electronics Engineering Research Institute (CEERI), Pilani, India for access to Laser Doppler Vibrometer facility.

References

Ahmed A, Khlifi A, Pandit S, Patkar R, Joshi A, Dixit P, Mezghani B, Baghini MS (2020) Design, fabrication, and characterization of SU-8/carbon black nanocomposite based polymer MEMS acceleration sensor, Microsyst Technol.

Alvin Barlian A, Park W-T, Mallon Jr JR, Rastegar AJ, Pruitt BL (2009) Review: semiconductor piezoresistance for Microsystems. In: Proc. IEEE Vol. 97, pp. 513

Available online: http://www.microchem.com/Prod-SU8_KMPR.html

Aydemir A, Akin T (2020) Self-packaged three axis capacitive mems accelerometer. In: IEEE 33rd International Conference on Micro Electro Mechanical Systems (MEMS), Vancouver, BC, Canada, pp. 777–780.

Bao M-H (2000) Micro mechanical transducers: pressure sensors, accelerometers and gyroscopes. In: Middelhoek S (ed) Handbook of Sensors and Actuators, vol. 8, Elsevier, Oxford

Carreno AAA, Conchouso D, Zaher A, Foulds I, Kosel J (2013) Simulation of a Low Frequency Z-Axis SU-8 Accelerometer in CoventorWare and MEMS+. In: 2013 UKSim 15th International Conference on Computer Modelling and Simulation, Cambridge, pp. 792–797.

Chen F, Li X, Kraft M (2016) Electromechanical sigma-delta modulators (ΣΔM) force feedback interfaces for capacitive MEMS inertial sensors: a review. IEEE Sens J 16(17):6476

Chung S, Park S (2013) Effects of temperature on mechanical properties of SU-8 photoresist material. J Mech Sci Technol 27(9):2701

Fan X, et al (2020) Manufacture and characterization of graphene membranes with suspended silicon proof masses for MEMS and NEMS applications. Microsyst Nanoeng 6(17)

Gong X, Wu W-J, Liao W-H (2020) A low-noise three-axis piezoelectric MEMS accelerometer for condition monitoring. Proc SPIE 11379:113790U

Hassani FA, Payam AF, Fathipour M (2010) Design of a smart MEMS accelerometer using nonlinear control principles. Smart Struct Syst 6(1):1–16

Hurst AM, Lee S, Cha W, Hone J (2015) A graphene accelerometer. In: 2015 28th IEEE International Conference on Micro Electro Mechanical Systems (MEMS), Estoril, pp. 865–868.

Jeong SJ, Wang W (2004) Microaccelerometers using cured SU-8 as structural material. In: Proc. SPIE 5344, MEMS/MOEMS components and their applications

Jiang L, Cheung R (2009) A review of silicon carbide development in MEMS applications. Int J Computat Mater Sci Surf Eng 2(3/4): 227

Kim BJ, Meng E (2016) Review of polymer MEMS micromachining. J Micromech Microeng 26(1):013001

Kobayashi T, Okada H, Masuda T, Maeda R, Itoh T (2011) A digital output accelerometer using MEMS-based piezoelectric accelerometers and arrayed CMOS inverters with satellite capacitors. Smart Mater Struct 20(6):065017

Kraft M (2000) Micromachined inertial sensors state of the art and a look into the future. IMC Meas Control 33(6):164

Kumar V, Jafari R, Pourkamali S (2016) Ultra-low power digitally operated tunable MEMS accelerometer. IEEE Sens J 16(24):8715

Kwon K, Park S (1998) A bulk-micromachined three-axis accelerometer using silicon direct bonding technology and polysilicon layer. Sens Actuat A 66:250–255

Lapadatu D, Pyka A, Dziuban J, Puers R (1996) Corrugated silicon nitride membranes as suspensions in micromachined silicon accelerometers. J Micromech Microeng 6:73–76

Lawes RA (2007) Manufacturing costs for microsystems/MEMS using high aspect ratio microfabrication techniques. Microsyst Technol 13:85

Liu G, Yang F, Bao X, Jiang T (2015) Robust optimization of a MEMS accelerometer considering temperature variations. Sensors 15(3):6342

Llobera A, Seidemann V, Plaza JA, Cadarso VJ, Buttgenbach S (2007) SU-8 optical accelerometers. J Microelectromech Syst 16(1):111

Madou M (1997) Principal source for semiconductor material properties: "fundamentals of microfabrication". CRC Press

Michel SJ (2004) Market opportunities for advanced MEMS accelerometers and overview of actual capabilities vs. required specifications. In: PLANS 2004, Position Location and Navigation Symposium (IEEE Cat. No.04CH37556), Monterey, CA, USA, pp. 78

Milligan DJ, Hom BD, Walmsley RG (2011) An ultra-low N noise MEMS accelerometer for seismic imaging. IEEE Sens J:1–4

Mohamad N (2010) Modelling and optimisation of a spring-supported diaphragm capacitive MEMS microphone. Engineering 2(10):762

Monajemi P, Ayazi F (2006) Design optimization and implementation of a microgravity capacitive HARSS accelerometer. IEEE Sens J 6(1):39

Narasimhan V, Li H, Jianmin M (2015) Micromachined high-g accelerometers: a review. J Micromech Microeng 25:033001

Oliver W, Pharr G (2004) Measurement of hardness and elastic modulus by instrumented indentation: advances in understanding and refinements to methodology. J Mater Res 19(1):3

Paul T, Singh J, Nayak MM, Rajanna K, Kumar MS (2008) Design and optimization of bulk micromachinaded accelerometer for space applications. Int J Smart Sens Intell Syst 1(4):1019

Qu H, Fang D, Xie H (2004) A single-crystal silicon 3-axis CMOS-MEMS accelerometer. In: proceedings of IEEE Sensor vol. 2, pp 661.

Qu H, Fang D, Xie H (2008) A monolithic CMOS-MEMS 3-axis accelerometer with a low-noise, low-power dual-chopper amplifier. IEEE Sens J 8(9):1511

Rajgopal S, Zula D, Garverick S, Mehregany M (2009) A silicon carbide accelerometer for extreme environment applications. Mater Sci Forum 600–603:859–862

Rammohan A, Dwivedi PK, Duarte RM, Katepalli H, Madou MJ, Sharma A (2011) One-step maskless grayscale lithography for the fabrication of 3-dimensional structures in SU-8. Sens Actuat B 153:125

Rao K, et al (2020) A High-resolution area-change-based capacitive MEMS accelerometer for tilt sensing. In: IEEE International Symposium on Inertial Sensors and Systems (INERTIAL), Hiroshima, Japan, pp. 1-4

Roy AL, Bhattacharyya TK (2015) Design, fabrication and characterization of high performance SOI MEMS piezoresistive accelerometers. Microsyst Technol 21(1):55

Roylance LM, Angell J (1979) Batch-fabricated silicon accelerometer. IEEE Trans Electron Devices 26(12):1911

Maier-Schneider DA, Koprululu S, Ballhausen Holm, and Obermeier E (1996) Elastic properties and microstructure of LPCVD polysilicon films. J Micromech Microeng 6(4)

Omeltchenko A, Nakano A, Kalia RK, and Vashishta P (1996) Structure, mechanical properties, and thermal transport in microporous silicon nitride–molecular-dynamics simulations. EPL (Europhys Lett) 33(9)

Seena V, Hari K, Prajakta S, Pratap R, Rao VR (2017) A novel piezoresistive polymer nanocomposite MEMS accelerometer. J Micromech Microeng 27:015014

Soni M, Arora T, Khosla R, Kumar P, Soni A, Sharma SK (2016) Integration of highly sensitive oxygenated graphene with aluminum micro-interdigitated electrode array based molecular sensor for detection of aqueous fluoride anions. IEEE Sens J 16(6):1524

Spearing SM (2000) Materials issues in Microelectromechanical system (MEMS). Acta mater 48:179

Suzuki YS, Tai Y (2006) Micromachined high-aspect-ratio parylene spring and its application to low-frequency accelerometers. J Microelectromech Syst 15(5):1364

Taghavi M, Latifi H, Parsanasab GM, Abedi A, Nikbakht H, Sharifi MJ (2019) Simulation, fabrication, and characterization of a sensitive SU-8-based Fabry-Pérot MOEMS accelerometer. J Lightw Technol 37:1893

Xie H, Fedder GK (2000) A CMOS Z-axis capacitive accelerometer with comb finger sensing. In: IEEE Conference USA

Xie H, Fedder GK (2000) A CMOS Z-axis capacitive accelerometer with comb finger sensing. IEEE Conference USA

Yang Z, Yan G, Hap Y, Wu G (2004) Design and fabrication of a torsional z-axis capacitive accelerometer with novel comb capacitor. In: proceedings of 7th International Conference on Solid-State and Integrated Circuits Technology, vol. 3, pp 1792.

Yazdi N, Ayazi F, Najafi K (1998) Micromachined inertial sensors. Proc IEEE 86:1640

Yi T, Kim C (1999) Measurement of mechanical properties for MEMS materials. Measur Sci Technol 10(8)

Zhao J, Jia J, Wang H, Li W (2007) A novel threshold accelerometer with postbuckling structures for airbag restraint systems. IEEE Sens 7:1102–1109

Zhou X, Che L, Liang S, Lin Y, Li X, Wang Y (2015) Design and fabrication of a MEMS capacitive accelerometer with fully symmetrical double-sided H-shaped beam structure. J Micromech Microeng 131:51